GB-ArcSAR Imaging Based on Optimized Construction of Reference Plane

Yunkai Deng, Hanpu Zhou, Weiming Tian, *Member, IEEE*, Xin Xie, and Cheng Hu

***Abstract*—Due to the specific arc-scanning way of ground-based arc-scanning synthetic aperture radar (GB-ArcSAR) to synthesize aperture, when a target's height is large enough and deviates much from the reference imaging plane, the image defocus would occur since that the target's range migration trajectory cannot be completely compensated. This article makes a theoretical analysis of the reasons for GB-ArcSAR imaging defocus, when it is utilized to observe those targets with large height differences, i.e., large elevation angles, from the imaging plane. A quantitative relationship between the imaging defocus level and the elevation angle is deduced with the simulation of an ideal target. Aiming at solving the problem of imaging defocus, an optimized imaging method of GB-ArcSAR based on the reference plane construction is proposed. A series of reference planes with different inclination angles or starting ranges are constructed and utilized for radar imaging separately. The minimum entropy criterion is then taken to search for the optimal plane. The qualitative and quantitative comparisons of the simulated and experimental datasets with other methods both prove the effectiveness of the proposed method.**

***Index Terms*—Ground-based arc-scanning synthetic aperture radar (GB-ArcSAR), image defocus, minimum entropy criterion, reference plane construction.**

I. Introduction

LANDSLIDES are the most frequent and harmful geological disasters. Deformation measurement is rather crucial for forecasting landslides of natural and engineered slopes [1], [2]. As a mature kind of noncontact and high-accuracy measurement instrument, ground-based synthetic aperture radar (GB-SAR) has been widely applied to measure surface deformation [3], [4].

Manuscript received 31 August 2023; revised 29 November 2023; accepted 6 January 2024. Date of publication 26 January 2024; date of current version 13 February 2024. This work was supported in part by National Key Research and Development Project under Grant 2021YFC3001903, in part by the Foundation of China State Construction Engineering Corporation under Grant CSCEC-2022-Z-4, in part by the National Natural Science Foundation of China under Grant 62101036, and in part by the Beijing Institute of Technology Research Fund Program for Young Scholars. *(Corresponding author: Weiming Tian.)*

Yunkai Deng is with the Radar Research Lab, School of Information and Electronics, Beijing Institute of Technology, Beijing 100081, China (e-mail: yunkai_bit@foxmail.com).

Hanpu Zhou and Xin Xie are with the Key Laboratory of Electronic and Information Technology in Satellite Navigation (Beijing Institute of Technology), Ministry of Education, Beijing 100081, China (e-mail: 451198964@qq.com; 3120215409@bit.edu.cn).

Weiming Tian is with the Beijing Institute of Technology Chongqing Innovation Center, Chongqing 401120, China (e-mail: tianwei6779@163.com).

Cheng Hu is with the Advanced Technology Research Institute, Beijing Institute of Technology, Jinan 250300, China (e-mail: cchchb@163.com).

Digital Object Identifier 10.1109/JSTARS.2024.3352287

Generic GB-SAR systems achieve a large synthetic aperture by moving the antennas along a linear track or adopt a multiple-input multiple-output structure, and they can only monitor scenes in the front direction [5], [6]. As a special kind of mechanical scanning GB-SAR system, ground-based arc-scanning synthetic aperture radar (GB-ArcSAR) achieves its synthetic aperture based on controlling the antennas to scan circumferentially in the horizontal plane, which enables GB-ArcSAR to have omnidirectional monitoring capability [7].

However, the specific way to synthesize the aperture of GB-ArcSAR causes its two-dimensional (2-D) high-resolution imaging to be significantly different from the linear-scanning GB-SAR. Wang et al. proved that if a target's height is large enough and deviates much from the reference imaging plane, the decrease in imaging quality or image defocusing would occur since that the target's range migration trajectory cannot be compensated accurately.

To solve this imaging problem, Wang et al. [8] proposed to utilize the interferometric digital elevation model (DEM) to assist GB-ArcSAR imaging. With the assist of DEM, targets in a scene are imaged on their actual heights. However, the DEM is acquired by taking interferometric processing to two GB-ArcSAR images. When the measurement scene is a steep slope with large elevation differences from the imaging plane, the initial images are severely defocused and cannot be utilized for the DEM acquisition. Besides, their method is only validated with the simulation datasets.

In addition to the above research, many research articles on GB-ArcSAR are focused on the fast-imaging algorithms. Lee et al. [9] established the GB-ArcSAR imaging geometric model and proposed the time-domain imaging algorithm of focusing mode and the range Doppler imaging algorithm of scanning mode. Luo et al. [10], [11] proposed a fast-imaging algorithm based on constructing a matched filtering function of the target with the scene center. Some other frequency-domain imaging algorithms aimed at improving the imaging efficiency are also proposed [12], [13], [14]. However, most of them have not considered the impact of terrain on GB-ArcSAR imaging.

This article provides a theoretical analysis of the reasons for GB-ArcSAR imaging defocus, when it is utilized to observe those targets with large height differences, i.e., large elevation angles, from the imaging plane. A quantitative relationship between the imaging defocus level and the elevation angle is deduced with the simulation of an ideal target. Then, an optimized imaging method of GB-ArcSAR based on reference plane construction is proposed. A series of reference planes with

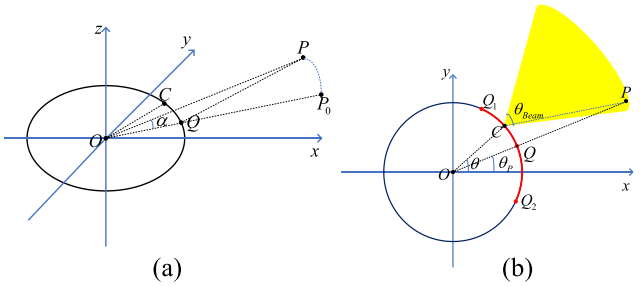

Fig. 1. (a) Imaging geometry of GB-ArcSAR. (b) Top view of the imaging geometry.

different inclination angles or staring ranges are constructed and utilized for imaging separately. The minimum entropy criterion is taken to search for the optimal plane. Both simulated and experimental datasets are used to verify the effectiveness of the proposed method and the potential of this method in interferometry applications.

II. Geometric Model and Defocus Analysis of GB-ArcSAR Imaging

A. Geometric Model

GB-ArcSAR achieves its synthetic aperture by controlling the transmitting and receiving antennas to periodically rotate in the horizontal plane. Fig. 1 shows the geometric model of GB-ArcSAR [15]. The *O-xy* plane is the rotation plane, *z*-axis is the rotation axis, and O is the rotation center. C denotes the antenna position, r is its rotation radius, and θ is its azimuth angle. Then, the antenna's coordinate is $(r\cos\theta, r\sin\theta, 0)$.

For a target P with the slant range of R from the center O, azimuth angle of θ_p, and elevation angle of α, its coordinate in the Cartesian coordinate system can be expressed as

$$(R\cos\alpha\cos\theta_P, R\cos\alpha\sin\theta_P, R\sin\alpha) \tag{1}$$

θ_{Beam} is the beamwidth. The arc $\overset{\frown}{Q_1Q_2}$ in Fig. 1(b) denotes the antenna scanning trajectory where the target *P* could be observed. Take the rotating plane *O-xy* as the imaging plane. Assuming P_0 to be the projection point of P on the imaging plane, P_0 has the same azimuth angle θ_p with P and satisfies the range equation $R_{QP} = R_{QP_0}$, where *Q* is at the intersection of the line *OP* and the arc $\overset{\frown}{Q_1Q_2}$ from the top view. *Q* is also the midpoint of $\overset{\frown}{Q_1Q_2}$. Then, the coordinate of P_0 can be expressed as

$$(R_{OP_0}\cos\theta_P, R_{OP_0}\sin\theta_P, 0) \tag{2}$$

where $R_{OP_0} = \sqrt{r^2+R^2-2rR\cos\alpha}+r$. When the height of P is zero ($\alpha = 0°$), P and P_0 are overlapping.

For the target *P*, when the antennas rotate from Q_1 to Q_2, the ranges between them are variant, and it is called the range migration curve, which is a rather important concept for SAR imaging.

For those targets with the same slant range from the center O and the same height from the rotation plane *O-xy*, even if their azimuth angles are different, they still have the same range migration curves. Therefore, the analysis problem of the imaging geometry model can be simplified by setting θ_p to be 0°. For any observation moment, the slant range R_{CP} between the antenna position *C* and the target *P* is

$$R_{CP} = \sqrt{r^2+R^2-2rR\cos\alpha\cos\theta}. \tag{3}$$

The slant range R_{CP_0} between *C* and the projection point P_0 is

$$R_{CP_0} = \sqrt{r^2+R_{OP_0}^2-2rR_{OP_0}\cos\theta}. \tag{4}$$

B. Defocus Analysis

The time-domain backprojection (BP) algorithm is utilized to take defocus analysis of GB-ArcSAR imaging [9]. Taking the linear frequency-modulated signal as an example, the echo signal of the target P can be expressed as

$$\begin{aligned} S_{rc}(t,\theta) = {} & \text{rect}\left(\frac{\theta-\theta_P}{\theta_{\text{Beam}}}\right)\cdot\text{rect}\left(\frac{t-\frac{2R_{CP}}{c}}{T_p}\right) \\ & \cdot\exp\left[j\pi K\left(t-\frac{2R_{CP}}{c}\right)^2+j2\pi f_c\left(t-\frac{2R_{CP}}{c}\right)\right] \end{aligned} \tag{5}$$

where t is the signal sampling time, c is the light speed, T_p is the signal pulsewidth, K is the frequency-modulated rate, and f_c is the carrier frequency.

The signal after pulse compression is expressed as

$$\begin{aligned} S_{\text{out}}(t,\theta) = {} & \text{rect}\left(\frac{\theta-\theta_P}{\theta_{\text{Beam}}}\right) \\ & \cdot\text{sinc}\left[KT_p\left(t-\frac{2R_{CP}}{c}\right)\right]\cdot\exp\left(-j\frac{4\pi R_{CP}}{\lambda}\right) \end{aligned} \tag{6}$$

where the last term is the Doppler phase term. For the target *P*, in order to realize coherent integral and azimuth focusing, phase compensation is required. The phase term utilized to compensate the Doppler phase term in (6) is calculated with the range migration curve of P_0 and is expressed as

$$H(\theta,t) = \exp\left(j\frac{4\pi R_{CP_0}}{\lambda}\right). \tag{7}$$

Therefore, the imaging result of P on the imaging plane is

$$\begin{aligned} I_{P_0} = {} & \sum_{\theta=\theta_P-\theta_{\text{Beam}}/2}^{\theta_P+\theta_{\text{Beam}}/2}\text{sinc}\left[KT_p\left(t-\frac{2R_{CP}}{c}\right)\right] \\ & \cdot\exp\left[-j\frac{4\pi\left(R_{CP_0}-R_{CP}\right)}{\lambda}\right]. \end{aligned} \tag{8}$$

However, the range migration curves R_{CP} and R_{CP_0} are inconsistent when the target *P* has a height deviating from the imaging plane. Therefore, the Doppler phase in (6) cannot be accurately compensated, resulting in a decrease in the imaging quality or even defocusing [16]. The difference curve ΔR between R_{CP} and R_{CP_0} is defined as

$$\Delta R = \left|R_{CP_0}-R_{CP}\right|. \tag{9}$$

When the rotation radius is fixed, ΔR is affected by the elevation angle α and the slant range R of the target. Table I presents the simulation parameters. Three elevation angles of 10°, 30°, and 50° and two slant ranges of 500 m and 1000 m are set.

TABLE I
SIMULATION PARAMETERS

Parameter	Value	Parameter	Value
Signal form	Frequency-modulated continuous wave	Pulse repetition time	0.5 ms
Center frequency	16.2 GHz	Signal duration	0.5 ms
Rotating arm length	1.2 m	Bandwidth	800 MHz
Sampling rate	20 MHz	Beamwidth	40°

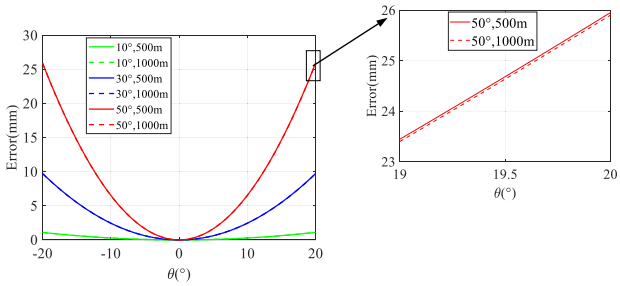

Fig. 2. Range migration difference curves of six targets.

Fig. 2 shows the range migration difference curves of six targets, with different elevation angles or slant ranges. The image on the right shows a locally enlarged view. It can be noted that, for two targets with the same elevation angle, their curves are almost the same and not variant with the slant ranges. When the azimuth angle of the antenna θ equals 0°, i.e., the azimuth angle of the target P, $\Delta R = 0\,\mathrm{m}$. As the antenna deviates from the target P in the azimuth angle, the range migration difference ΔR gradually increases. Besides, ΔR reaches its maximum value when the antenna reaches the edge observation position Q_1 or Q_2.

Define the maximum value of ΔR as ΔR_m

$$\Delta R_m = \left| \begin{array}{l} \sqrt{r^2 + R_{OP_0}^2 - 2rR_{OP_0}\cos\frac{\theta_{\mathrm{Beam}}}{2}} \\ -\sqrt{r^2 + R^2 - 2rR\cos\alpha\cos\frac{\theta_{\mathrm{Beam}}}{2}} \end{array} \right|. \quad (10)$$

When $r = 1.2\,\mathrm{m}$ and $\theta_{\mathrm{Beam}} = 40°$, the variation map of ΔR_m with the slant range R and the elevation angle α is shown in Fig. 3(a), whose variation range is from 0 to 40 mm. Two 1-D cross-sectional lines are used to better show the variation of ΔR_m with R and α. Fig. 3(b) shows that when α is fixed, ΔR_m is almost a constant and less affected by R. Fig. 3(c) shows that, as α increases, ΔR_m gradually increases. When $\alpha = 60°$, ΔR_m increases to a rather large value of 36.29 mm. Three different error values of $\lambda/16$, $\lambda/8$, and $\lambda/4$ are marked, where λ is calculated with the parameters in Table I, and the corresponding elevation angles are 10.2°, 14.5°, and 20.6°.

Fig. 4 shows the simulated imaging results of four targets with different values of α and the same slant range R. Fig. 4(a) is the ideal result with perfect focus and can be used to qualitatively compare with other imaging results. The target's defocusing level in Fig. 4(b) cannot be observed visually, which indicates that the defocusing threshold of $\lambda/16$ could be rather harsh. Correspondingly, the defocusing levels of Fig. 4(c) and (d) are

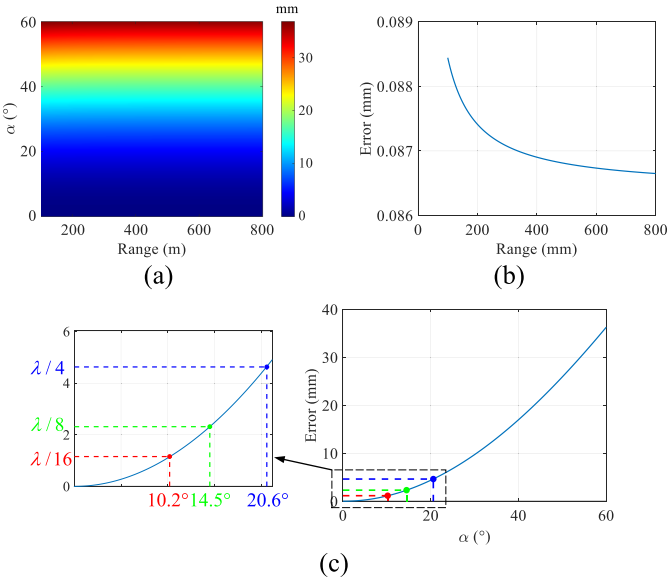

Fig. 3. (a) Variation map of ΔR_m with the slant range R and the elevation angle α. (b) Variation curve of ΔR_m with R. (c) Variation curve of ΔR_m with α.

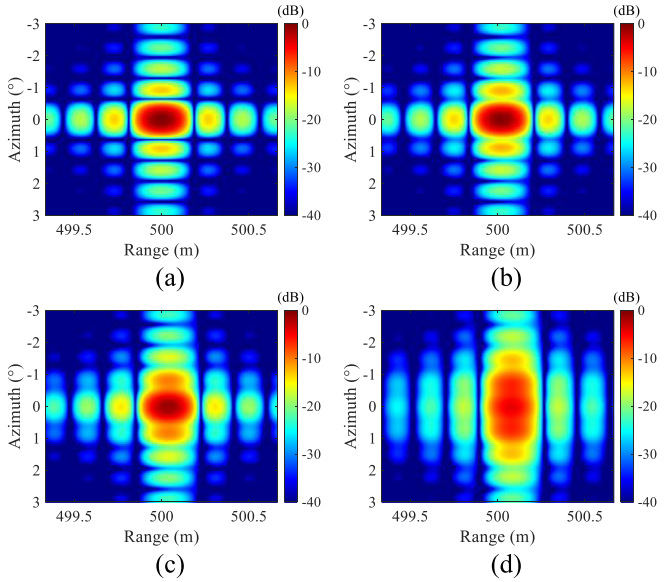

Fig. 4. Simulated imaging results of four targets with the same range R and different values of α. (a) $\alpha = 0°$. (b) $\alpha = 10.2°$. (c) $\alpha = 14.5°$. (d) $\alpha = 20.6°$.

severe, especially in the azimuth dimension. To quantitatively evaluate the imaging quality of these maps, some indicators, including the peak strength, resolution, integrated sidelobe ratio (ISLR), and peak-to-sidelobe ratio (PSLR), both in the range and azimuth dimensions are utilized.

For the four maps in Fig. 4, the range and azimuth profiles of their peak pixels are shown in Fig. 5, respectively. Table II also gives the quantitative comparisons. The slant range of the peak pixel in Fig. 5(a) has been corrected to be the same. The resolutions and PSLRs and ISLRs for different α in the range dimension are almost the same, with only a decrease in peak strength. When $\alpha = 14.5°$, the peak strength only decreases

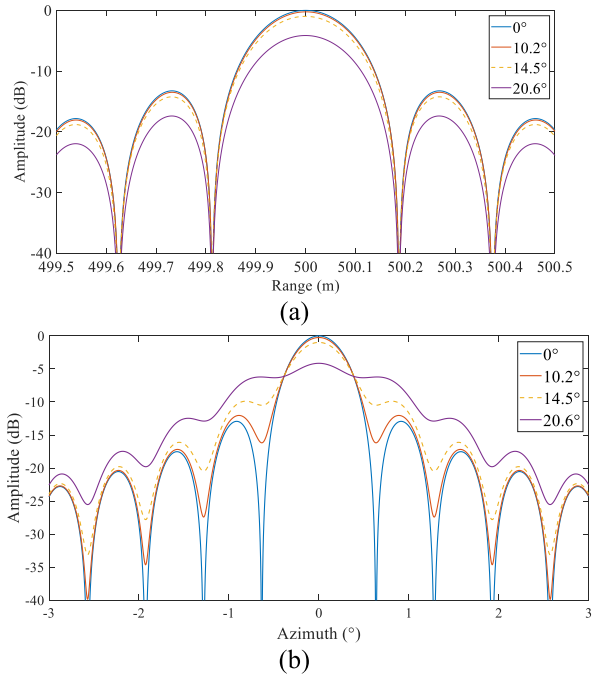

Fig. 5. Range and azimuth profiles of the peak pixels in Fig. 4. (a) Range profile. (b) Azimuth profile.

TABLE II
QUANTITATIVE COMPARISONS OF THE IMAGING RESULTS OF FOUR TARGETS WITH DIFFERENT α

ΔR_m	0	$\lambda/16$	$\lambda/8$	$\lambda/4$
α (°)	0	10.2	14.5	20.6
Peak Strength (dB)	0	-0.24	-0.98	-4.14
Range Resolution (m)	0.1661	0.1661	0.1661	0.1661
Range PSLR (dB)	−13.26	−13.26	−13.26	−13.26
Range ISLR (dB)	-11.16	-11.18	-11.19	-11.19
Azimuth Resolution(°)	0.5611	0.57	0.606	1.7101
Azimuth PSLR (dB)	-12.93	-11.88	-8.42	-2.06
Azimuth ISLR (dB)	-10.65	-10.53	-10.47	-10.22

by 0.98 dB. However, the resolutions and PSLRs and ISLRs for different α in the azimuth dimension become worse with the increase of α. When $\alpha = 10.2°$, the azimuth resolution deteriorates by 1.6%, and the PSLR increases by 1.05 dB, and the ISLR increases by 0.12 dB. The loss of the azimuth focusing performance can be negligible. When $\alpha = 14.5°$, the azimuth resolution deteriorates by 8%, and the PSLR increases by 4.51 dB. The loss of the azimuth focusing performance can be accepted to some extent. However, when $\alpha = 20.6°$, the azimuth profile is completely defocused, making it difficult to distinguish between the main and side lobes.

Based on the above analysis, it can be noted that when a target's elevation angle is large enough and deviates much from the reference imaging plane, the decrease of the GB-ArcSAR focusing performance in the azimuth dimension cannot be avoided and gradually deteriorate as the elevation angle increases. The fundamental reason is due to the specific arc-scanning way of GB-ArcSAR to synthesize aperture. When a target deviates from the reference imaging plane, its actual range migration curve cannot be completely consistent with any projection point on the reference imaging plane. Therefore, the compensated phase term in (8) is nonzero and causes an incomplete coherent accumulation, resulting in a decrease in the azimuth focusing.

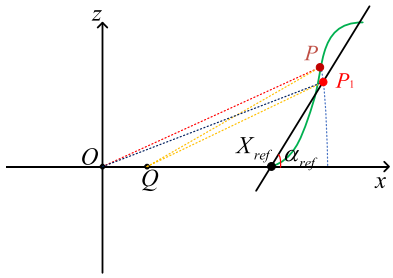

Fig. 6. Side view of the GB-ArcSAR imaging geometry.

III. REFERENCE PLANE CONSTRUCTION METHOD

When the GB-ArcSAR system is utilized to monitor slopes or buildings, and the zero-height rotation plane is used as the imaging reference plane, the imaging defocus level of those targets with large elevation angles would be severe. To solve this problem, a GB-ArcSAR imaging method based on the optimized construction of reference imaging plane is proposed. By reducing the maximum difference of the range migration curves between those targets and their projection points on the reference plane, the imaging focus performance could be well increased. To a certain extent, the reference imaging plane can be regarded as an approximation of the slope terrain or the building structure.

A. Reference Plane Analysis

Fig. 6 shows the side view of the GB-ArcSAR imaging geometry. The green curve represents a slope, and the black line is the reference imaging plane at X_{ref} with the elevation angle of α_{ref}. P denotes a target with the azimuth angle 0°, elevation angle α_P, and range $|OP| = R$. The coordinate of P is $(R\cos\alpha_P, 0, R\sin\alpha_P)$. Q is the midpoint of $\overset{\frown}{Q_1Q_2}$, as shown in Fig. 1.

Assume that the projection point of P on the reference imaging plane is P_1 and the coordinate of P_1 is $(x_{P1}, 0, z_{P1})$

$$z_{P1} = (x_{P1} - X_{\text{ref}})\tan\alpha_{\text{ref}}. \tag{11}$$

The equation $|QP| = |QP_1|$ is satisfied. It can be obtained that

$$(R\cos\alpha_P - r)^2 + (R\sin\alpha_P)^2 = (x_{P1} - r)^2 + z_{P1}^2. \tag{12}$$

Combining (11) and (12), we can get the projection position P_1 of P on the reference imaging plane. The elevation angle

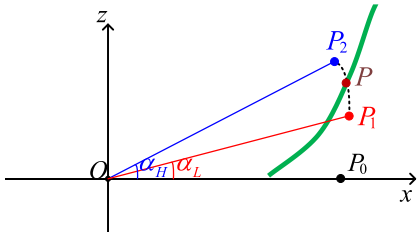

Fig. 7. Schematic diagram of the upper and lower imaging boundaries.

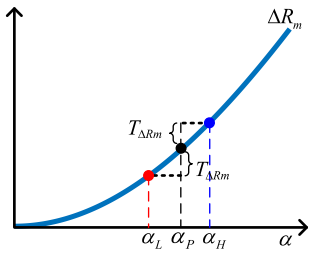

Fig. 8. Schematic diagram for solving the boundary angles.

difference between the target and its projection point becomes small. Then, the maximum value ΔR_m of their range migration difference curves could be reduced. By taking SAR imaging to P on this new reference plane rather than the radar rotation plane, the defocus level can be well reduced.

For any target P in 3-D space, the upper boundary α_H and lower boundary α_L can be used to describe the projection positions without defocusing, as shown with the black dotter arc $\widehat{P_1P_2}$ in Fig. 7. P_0 denotes the projection position of P on the radar rotation plane. It should be noted that P, P_0, P_1, and P_2 have the same range from the midpoint Q of the antenna scanning trajectory Q_1Q_2 determined by the target P and the antenna beamwidth.

Due to the complexity of the expression ΔR_m in (10), it is difficult to directly calculate the two boundary angles α_H and α_L. A defocus threshold $T_{\Delta Rm}$ about the maximum value ΔR_m of the range migration difference in (10) can be defined. Here, we just utilize this threshold to judge whether the imaging defocus level of a target can be accepted or not. The above analysis result illuminates that $T_{\Delta Rm} = \lambda/8$ might be a good choice. Based on the defocus threshold $T_{\Delta Rm}$, α_L and α_H can be searched

$$\begin{aligned} \Delta R_m(\alpha_L) &= \min\left(\Delta R_m(\alpha_P) - T_{\Delta Rm}, 0\right) \\ \Delta R_m(\alpha_H) &= \Delta R_m(\alpha_P) + T_{\Delta Rm}. \end{aligned} \tag{13}$$

For the target *P*, we can project it onto a series of planes with the same starting position X_{ref} and different inclination angles α. Then, calculate the projection position on each imaging plane and the corresponding $\Delta R_m(\alpha)$. α_L and α_H can be obtained according to (14). Fig. 8 shows the diagram for solving the boundary angles.

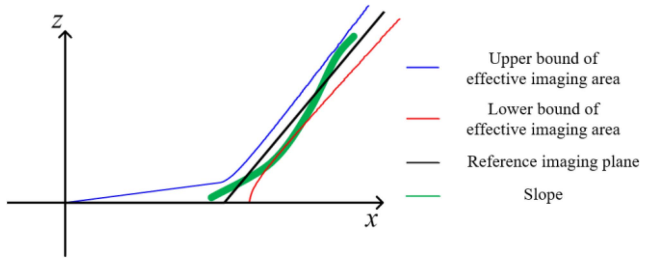

Fig. 9. Reference imaging plane of a simple slope.

B. Optimized Construction of Reference Plane

For any target P in 3-D space, if it is on a plane and its slant range and azimuth directions are orthogonal to the normal of the plane, P can be perfectly focused on this imaging plane with GB-ArcSAR. The above analysis on a single target has proved that the defocus level could be negligible even if P deviates from the imaging plane within a certain angle range. Therefore, for a simple actual scene, such as a linear slope or a single building, one 2-D imaging plane can be constructed to simulate its terrain or structure. The green curve in Fig. 9 represents a slope, and the black line is the reference imaging plane. The blue and red lines jointly constitute the effective imaging area of the reference plane, whose basic principle is shown in Fig. 6 and the acquisition method is calculated with (14).

A problem to be further solved is to determine the two parameters X_{ref} and α_{ref}, which are utilized to describe the reference plane, as shown in Fig. 6. For a building, set α_{ref} to be 90° and search for the optimal X_{ref}. For a slope, set X_{ref} to be the minimum range from radar to the slope according to the echo signals and search for the optimal α_{ref}. A series of imaging planes with different parameters X_{ref} or α_{ref} based on the scene type can be constructed, and each plane is utilized for GB-ArcSAR imaging. Then, to select the optimal imaging reference plane, the minimum entropy optimization criterion is utilized to evaluate the imaging quality [17].

Assume that the size of the radar image is $N \times M$ and the complex information of the (n, m) pixel is represented as $I(n, m)$. The image entropy E is defined as

$$\begin{aligned} E &= -\sum_{n=1}^{N}\sum_{m=1}^{M} p(n,m)\log_{10} p(n,m) \\ p(n,m) &= \frac{|I(n,m)|^2}{P} \\ P &= \sum_{n=1}^{N}\sum_{m=1}^{M} |I(n,m)|^2 \end{aligned} \tag{14}$$

where P is the total power of the image, and $p(n, m)$ is the proportion of the (n, m) pixel in the total power of the image.

When $p(n, m) = 1/(N \cdot M)$, the energy of the image is evenly distributed on each pixel, and the image entropy is the largest. When the image is severely defocused, the energy distribution is relatively uniform, resulting in a higher image entropy. Therefore, the image entropy can be used as a standard

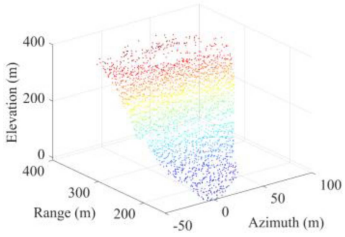

Fig. 10. Simulated slope.

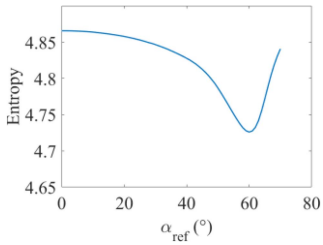

Fig. 11. Image entropy curve.

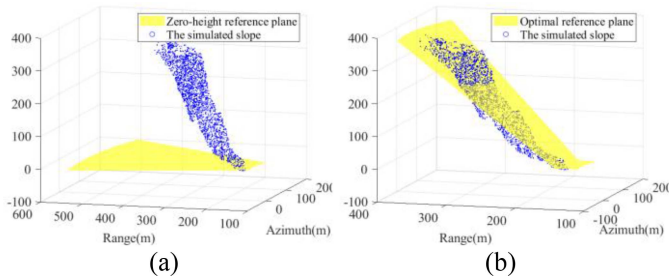

Fig. 12. Comparisons of two different reference planes. (a) Zero-height reference plane. (b) Optimal reference plane.

for the image quality evaluation. The smaller the image entropy, the better the focusing performance of radar images.

IV. Data Validation

A. Simulation Results

The simulation parameters of the GB-ArcSAR system are given in Table I. Fig. 10 shows the simulated slope with a minimum pitch angle of 3.7° and a maximum pitch angle of 46°.

Set $x_0 = 165\,\mathrm{m}$ and search for α_{ref} from 0° to 70°. We can get a series of SAR images with different imaging planes. The image entropy curve is shown in Fig. 11. When $\alpha_{\mathrm{ref}} = 60°$, the image entropy is minimum, and this plane is the optimal imaging reference plane.

Fig. 12 shows the simulated slope and two different imaging planes. It can be noted that the optimal imaging plane can well fit the terrain.

Comparisons of the imaging results with the above two imaging planes are shown in Fig. 13. Fig. 13(a) shows that when using a zero-height imaging reference plane, the defocus degree of the SAR images gradually becomes severe as the pitch angle increases. Fig. 13(b) shows that the SAR image is well focused when the optimal imaging reference plane is used. Fig. 13(c) and (d) compares the focusing effect of the slope toe area. Fig. 13(e) and (f) compares the focusing effect of the slope top area. Only the results with the optimal reference plane are well focused in both areas.

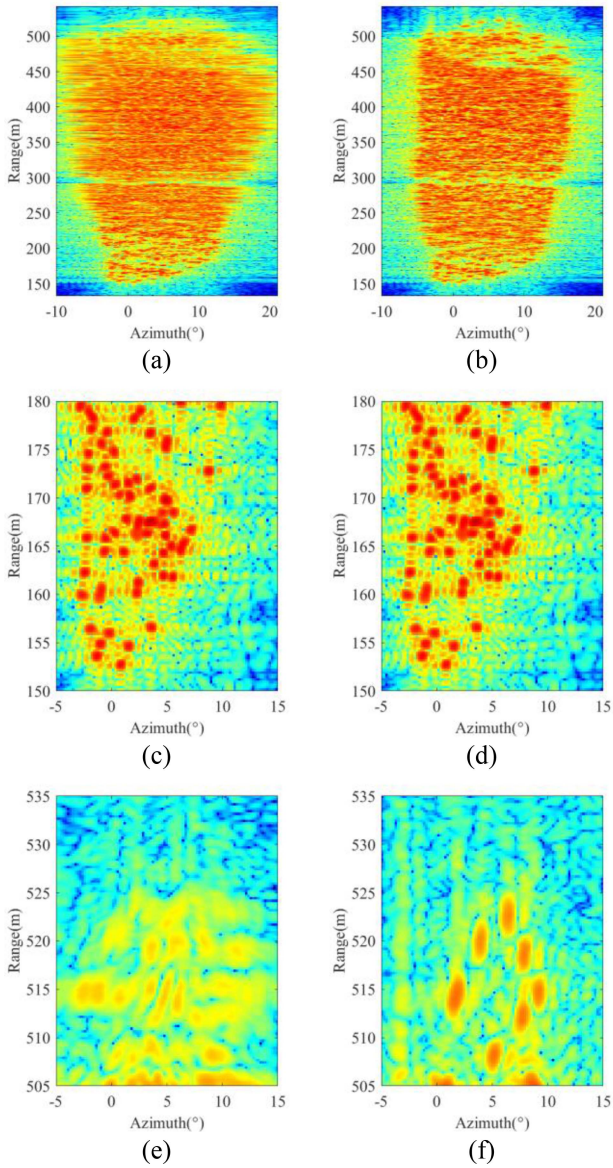

Fig. 13. Comparisons of the imaging results with two different imaging planes. Left column: zero-height reference plane. Right Column: optimal reference plane. (a) and (b) show the whole image. (c) and (d) show the slope toe area. (e) and (f) show the slope top area.

B. Experimental Results

Fig. 14 shows the GB-ArcSAR system developed by the Radar Research Lab of Beijing Institute of Technology. Its main parameters are shown in Table I.

The imaging experiment was carried out at Beijing Olympic Tower, which is composed of five single towers with different diameters and heights. Its maximum building height is 244.85 m.

Fig. 14. Photo of the GB-ArcSAR system.

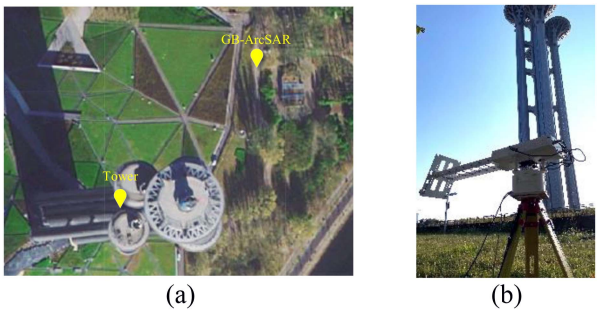

Fig. 15. (a) Experimental scenario. (b) Radar measurement geometry.

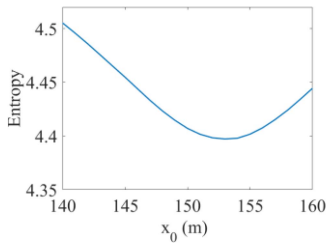

Fig. 16. Image entropy curve.

Each single tower consists of a polygonal tower body and a canopy-shaped viewing platform at the top. The photos of the experimental scenario and the radar measurement geometry are shown in Fig. 15.

The distance between the Beijing Olympic Tower and GB-ArcSAR is about 150 m. For buildings with vertical structures, set $\alpha_{\text{ref}} = 90^\circ$ and search for x_0 from 140 to 160 m. The image entropy curve is shown in Fig. 16. When $x_0 = 153\,\text{m}$, the image entropy gets its minimum value.

Fig. 17 shows the radar imaging results with three different reference planes. For Fig. 17(a), its image entropy is 4.65. Only a small number of pixels at the bottom of the tower have good focusing performance, while the rest pixels are almost completely defocused. For Fig. 17(b), its image entropy is 4.55. The imaging reference plane is constructed with a pitch angle of 40° and a starting range of $x_0 = 0\,\text{m}$. It is well focused only in the middle region of the tower. For Fig. 17(c), its image entropy is 4.39. The imaging reference plane is selected with the minimum entropy, whose pitch angle α_{ref} is 90° and starting range x_0 is 153 m. It can be noted that the outline of the tower

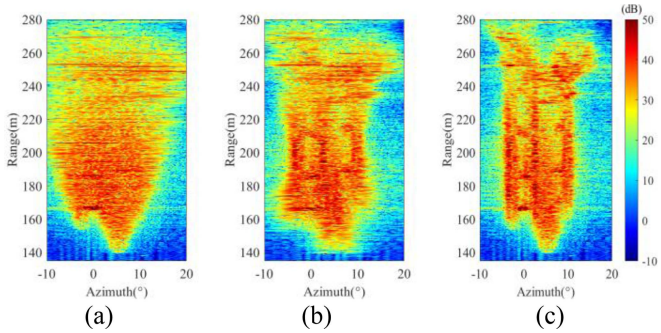

Fig. 17. Radar imaging results with three different reference planes. (a) Zero-height reference plane. (b) General imaging plane. (c) Optimal reference plane.

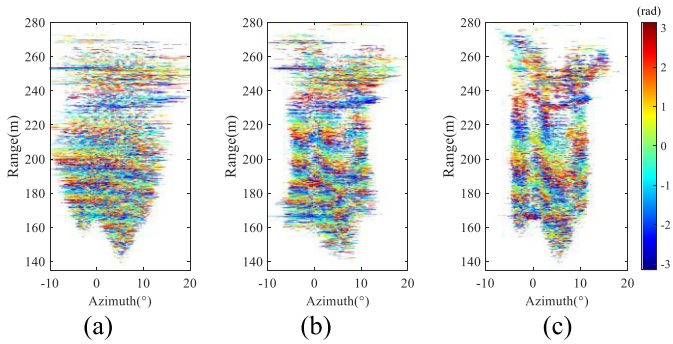

Fig. 18. Interferometric phase maps acquired based on Fig. 17. (a) Zero- height reference plane. (b) General imaging plane. (c) Optimal reference plane.

body is clear, and the connecting trusses between those towers are clearly visible. Therefore, the proposed method can also achieve good focus performance for buildings.

GB-ArcSAR can be utilized to take deformation monitoring or DEM generation [18], [19]. The antenna height is adjusted to obtain an interferometric baseline of about 10 cm. Fig. 18 shows the interferometric phase map of those pixels with large amplitude. Due to the image defocusing, the interferometric phase quality in Fig. 18(a) and (b) is poor. In Fig. 18(c), the interferometric fringes are obvious. Besides, it can be noted that the selected pixels are well located on the tower body. The above results indicate that the well-focused images with the proposed method can lay a good data foundation for the interferometric measurement.

V. Conclusion

This article aims at solving the defocus problem of GB-ArcSAR imaging for scenes with large heights and proposes an improved imaging method based on the optimized construction of reference plane. When the GB-ArcSAR imaging is taken on the external DEM with the BP algorithm, an optimal focused image can be acquired, but the proposed method proposed can achieve good focus performance of terrain with large heights' differences without the assistance of DEM.

The proposed method constructs different imaging reference planes and takes imaging on each plane with the BP algorithm. If N reference planes are constructed, the time complexity of

the proposed method is about N times of the traditional BP algorithm. As for the effect of the signal-to-noise ratio (SNR) on the proposed imaging method, since the GB-ArcSAR is commonly utilized to monitor buildings or slopes, pixels that could be utilized for interferometry or differential interferometry are sufficient enough and they typically have high SNRs about 10–30 dB in such scenes. Therefore, we have not considered the effect of the SNR on the proposed imaging method. The method can achieve good focusing performance for a single and simple scene. For scenes with multiple slopes or buildings, an image segmentation strategy can be adopted. Each slope and building can be imaged separately with the optimization method, and then the imaging result of the entire scene is obtained through the image fusion.

REFERENCES

[1] N. Casagli, F. Catani, C. D. Ventisette, and G. Luzi, "Monitoring, prediction, and early warning using ground-based radar interferometry," *Landslides*, vol. 7, no. 3, pp. 291–301, Sep. 2010, doi: 10.1007/s10346010-0215-y.

[2] R. Caduff, F. Schlunnegger, A. Kos, and A. Wiesmann, "A review of terrestrial radar interferometry for measuring surface change in the geosciences," *Earth Surf. Processes Landforms*, vol. 40, no. 2, pp. 208–228, Feb. 2015, doi: 10.1002/esp.3656.

[3] M. Pieraccini and L. Miccinesi, "Ground-based radar interferometry: A bibliographic review," *Remote Sens.*, vol. 11, no. 9, Apr. 2019, Art. no. 1029, doi: 10.3390/rs11091029.

[4] Y. Wang et al., "Ground-based differential interferometry SAR: A review," *IEEE Geosci. Remote Sens. Mag.*, vol. 8, no. 1, pp. 43–70, Mar. 2020, doi: 10.1109/MGRS.2019.2963169.

[5] C. Hu, M. Zhu, T. Zeng, W. Tian, and C. Mao, "High-precision deformation monitoring algorithm for GBSAR system: Rail determination phase error compensation," *Sci. China Inf. Sci.*, vol. 59, 2016, Art. no. 082307.

[6] C. Hu, Y. Deng, and W. Tian, "Multistatic ground-based differential interferometric MIMO radar for 3D deformation measurement," *Sci. China Inf. Sci.*, vol. 64, no. 12, Dec. 2021, Art. no. 227301, doi: 10.1007/s11432-021-3352-y.

[7] F. Viviani, A. Michelini, L. Mayer, and F. Conni, "IBIS-ArcSAR: An innovative ground-based SAR system for slope monitoring," in *Proc. IEEE Int. Geosci. Remote Sens. Symp.*, Valencia, Spain, 2018, pp. 1348–1351, doi: 10.1109/IGARSS.2018.8517702.

[8] Y. Wang, Y. Song, Y. Lin, Y. Li, Y. Zhang, and W. Hong, "Interferometric DEM-assisted high precision imaging method for ArcSAR," *Sensors*, vol. 19, no. 13, Jul. 2019, Art. no. 2921, doi: 10.3390/s19132921.

[9] H. Lee, J.-H. Lee, K.-E. Kim, N.-H. Sung, and S.-J. Cho, "Development of a truck-mounted arc-scanning synthetic aperture radar," *IEEE Trans. Geosci. Remote Sens.*, vol. 52, no. 5, pp. 2773–2779, May 2014, doi: 10.1109/TGRS.2013.2265700.

[10] Y. Luo, H. Song, R. Wang, Z. Xu, and Y. Li, "Signal processing of arc FMCW SAR," in *Proc. Conf. Proc. Asia-Pacific Conf. Synthetic Aperture Radar*, Tsukuba, Japan, 2013, pp. 412–415.

[11] Y. Luo, H. Song, R. Wang, Y. Deng, F. Zhao, and Z. Xu, "Arc FMCW SAR and applications in Ground monitoring," *IEEE Trans. Geosci. Remote Sens.*, vol. 52, no. 9, pp. 5989–5998, Sep. 2014, doi: 10.1109/TGRS.2014.2325905.

[12] Y. Lin, Y. Liu, Y. Wang, S. Ye, and Y. Zhang, "Frequency domain panoramic imaging algorithm for ground-based ArcSAR," *Sensors*, vol. 20, no. 24, Dec. 2020, Art. no. 7027, doi: 10.3390/s20247027.

[13] Y. Zhang, Y. Wang, Y. Wei, L. Zhao, and W. Bai, "Spherical wave decomposition based polar format algorithm for ArcSAR imaging," *IEEE Trans. Geosci. Remote Sens.*, vol. 59, no. 9, pp. 7547–7556, Sep. 2021, doi: 10.1109/TGRS.2020.3035678.

[14] Z. Gao, Y. Jia, S. Liu, and X. Zhang, "A 2-D frequency-domain imaging algorithm for ground-based SFCW-ArcSAR," *IEEE Trans. Geosci. Remote Sens.*, vol. 60, Mar. 2022, Art. no. 5225514, doi: 10.1109/TGRS.2022.3161660.

[15] Z. Lin, Y. Deng, W. Tian, Z. Zhao, and C. Hu, "Ground-based ArcSAR interferometry and sensitivity analysis," in *Proc. CIE Int. Conf. Radar (Radar)*, Haikou, China, 2021, pp. 154–158.

[16] Y. Shao, Z. Chen, and X. Wu, "Investigation on imaging performance of circular scanning synthetic aperture radar," in *Proc. 31st URSI Gen. Assem. Sci. Symp.*, Beijing, China, 2014, pp. 1–4, doi: 10.1109/URSI-GASS.2014.6929636.

[17] Q. Liu, Y. Luo, Q. Zhang, W. Hong, and T. Yeo, "Precision downward-looking 3D synthetic aperture radar imaging with sparse linear array and platform motion parameters estimation," *Remote Sens.*, vol. 10, no. 12, Dec. 2018, Art. no. 1957, doi: 10.3390/rs10121957.

[18] Y. Deng, C. Hu, W. Tian, and Z. Zhao, "A grid partition method for atmospheric phase compensation in GB-SAR," *IEEE Trans. Geosci. Remote Sens.*, vol. 60, May 2021, Art. no. 5206713, doi: 10.1109/TGRS.2021.3074161.

[19] M. Pieraccini and L. Miccinesi, "ArcSAR for detecting target elevation," *Electron. Lett.*, vol. 52, no. 18, pp. 1559–1560, Sep. 2016, doi: 10.1049/el.2016.2367.

Yunkai Deng was born in 1992. He received the B.S. and Ph.D. degrees in information and communication engineering from the Beijing Institute of Technology, Beijing, China, in 2014 and 2020, respectively.

He is an Assistant Professor with the School of Information and Electronics, Beijing Institute of Technology. His research interests include SAR image processing and DInSAR technology.

Hanpu Zhou was born in 2000. She received the B.S. degree in communication engineering from Hunan University, Changsha, China, in 2022. She is currently working toward the M.S. degree in information and communication engineering with Radar Research Laboratory, Beijing Institute of Technology, Beijing, China, in 2023.

Her research interests include SAR imaging and interferometry.

Weiming Tian (Member, IEEE) was born in 1983. He received the B.S. and Ph.D. degrees in information and communication engineering from the Beijing Institute of Technology, Beijing, China, in 2005 and 2010, respectively.

He is currently with the School of Information and Electronics, Beijing Institute of Technology. His research interests include synthetic aperture radar (SAR) system design and signal processing, bistatic SAR synchronization, and differential interferometric SAR technology.

Xin Xie was born in 1996. He received the B.S. degree in communication engineering from Zhengzhou University, Zhengzhou, China, in 2019. He is currently working toward the Ph.D. degree in information and communication engineering with Radar Research Laboratory, Beijing Institute of Technology, Beijing, China.

His research interests include SAR imaging and interferometry.

Cheng Hu was born in Hunan Province, China. He received the B.S. degree in electronic engineering from the National University of Defense Technology, Changsha, China, in 2003, and the Ph.D. degree in target detection and recognition from the Beijing Institute of Technology (BIT), Beijing, China, in 2009.

From 2006 to 2007, he was a Research Associate with Microwave Integrate System Laboratory, University of Birmingham, Birmingham, U.K. Since 2012, he has been an Associate Professor with the School of Information and Electronics, BIT. His research interests include the geosynchronous SAR, bistatic SAR imaging processing, and forward scatter-radar signal processing.